

Ultra-low magnetic damping of a metallic ferromagnet

Martin A. W. Schoen^{1,2}, Danny Thonig³, Michael L. Schneider¹, T. J. Silva¹, Hans T. Nembach¹, Olle Eriksson³, Olof Karis³ and Justin M. Shaw^{1*}

Magnetic damping is of critical importance for devices that seek to exploit the electronic spin degree of freedom, as damping strongly affects the energy required and speed at which a device can operate. However, theory has struggled to quantitatively predict the damping, even in common ferromagnetic materials^{1–3}. This presents a challenge for a broad range of applications in spintronics⁴ and spin-orbitronics that depend on materials and structures with ultra-low damping^{5,6}. It is believed that achieving ultra-low damping in metallic ferromagnets is limited by the scattering of magnons by the conduction electrons. However, we report on a binary alloy of cobalt and iron that overcomes this obstacle and exhibits a damping parameter approaching 10^{-4} , which is comparable to values reported only for ferrimagnetic insulators^{7,8}. We explain this phenomenon by a unique feature of the band structure in this system: the density of states exhibits a sharp minimum at the Fermi level at the same alloy concentration at which the minimum in the magnetic damping is found. This discovery provides both a significant fundamental understanding of damping mechanisms and a test of the theoretical predictions proposed by Mankovsky and colleagues³.

In recent decades, several theoretical approaches have attempted to quantitatively predict magnetic damping in metallic systems. One of the early promising theories was that of Kambersky, who introduced the so-called breathing Fermi-surface model^{9–11}. More recently, Gilmore and Stiles² as well as Thonig *et al.*¹² demonstrated a generalized torque correlation model that includes both intraband (conductivity-like) and interband (resistivity-like) transitions. The use of scattering theory to describe damping was later applied by Brataas *et al.*¹³ and Liu *et al.*¹⁴ to describe damping in transition metals. A numerical realization of a linear response damping model was implemented by Mankovsky³ for Ni–Co, Ni–Fe, Fe–V and Co–Fe alloys. For the Co–Fe alloy, these calculations predict a minimum intrinsic damping of $\alpha_{\text{int}} \approx 0.0005$ at a Co-concentration of 10% to 20%, but was not experimentally observed¹⁵.

Underlying this theoretical work is the goal of achieving new systems with ultra-low damping that are required in many magnonic and spin-orbitronics applications^{7,8}. Ferrimagnetic insulators such as yttrium–iron–garnet (YIG) have long been the workhorse for these investigations, because YIG films as thin as 25 nm have experimental damping parameters as low as 0.9×10^{-4} (ref. 16). Such ultra-low damping can be achieved in insulating ferrimagnets in part due to the absence of conduction electrons—and, therefore, the suppression of magnon–electron scattering. However, insulators cannot be used in most spintronic and spin-orbitronic applications, where a charge current through

the magnetic material is required, nor is the requirement of growth on gadolinium gallium garnet templates compatible with spintronics and complementary metal-oxide semiconductor (CMOS) fabrication processes. One proposed alternative class of materials are Heusler alloys, some of which are theoretically predicted to have damping parameters as low as 10^{-4} (ref. 17). Although such values have yet to be realized, damping parameters as low as 0.001 have been reported for Co_2FeAl ¹⁸ and NiMnSb ¹⁹. However, Heusler alloys have non-trivial fabrication constraints, such as high-temperature annealing, which are also incompatible with spintronic and CMOS device fabrication constraints.

In contrast, metallic ferromagnets such as 3d transition metals are ideal candidate materials for these applications, because high-quality materials can be produced at room temperature (RT) without the requirement of annealing. However, ultra-low damping is thought to be unachievable in metallic systems, because damping in conductors is dominated by magnon–electron scattering in the conduction band, resulting in a damping parameter well over an order of magnitude higher than those found in high-quality YIG.

Inspired by Mankovsky's theoretical prediction of ultra-low damping in the $\text{Co}_x\text{Fe}_{1-x}$ alloy system³, we systematically studied the compositional dependence of the damping parameter in $\text{Co}_x\text{Fe}_{1-x}$ alloys, including careful evaluation of spin-pumping and radiative damping contributions. Polycrystalline $\text{Co}_x\text{Fe}_{1-x}$ alloy films, 10 nm thick, were sputter-deposited at RT with Cu(3 nm)/Ta(3 nm) seed and capping layers. X-ray diffraction (XRD) reveals that the Co–Fe alloys exhibit a body-centred-cubic (bcc) phase over a Co-concentration of 0% to 60%, a face-centred-cubic (fcc) phase above 80% Co, and a mixed phase between 60% and 80% Co, in good agreement with the bulk phase diagram of this system. The damping parameter is determined from broadband ferromagnetic resonance (FMR) spectroscopy, which measures the susceptibility over frequencies spanning from 5 GHz to 40 GHz. An example of $S_{21}(H)$ vector-network-analyser transmission data is shown in Fig. 1a,b, together with fits to the complex susceptibility for the real and imaginary parts, respectively. The total damping parameter α_{tot} is determined from the frequency dependence of the linewidth obtained from these susceptibility fits, according to equation (1),

$$\Delta H = \frac{2h\alpha_{\text{tot}}}{g\mu_0\mu_B}f + \Delta H_0 \quad (1)$$

where μ_0 is the vacuum permeability, μ_B is the Bohr magneton, h is Planck's constant, g is the Landé g -factor, and ΔH_0 is the inhomogeneous linewidth.

¹Quantum Electromagnetics Division, National Institute of Standards and Technology, Boulder, Colorado 80305, USA. ²Institute of Experimental and Applied Physics, University of Regensburg, 93053 Regensburg, Germany. ³Department of Physics and Astronomy, University Uppsala, S-75120 Uppsala, Sweden. *e-mail: justin.shaw@nist.gov

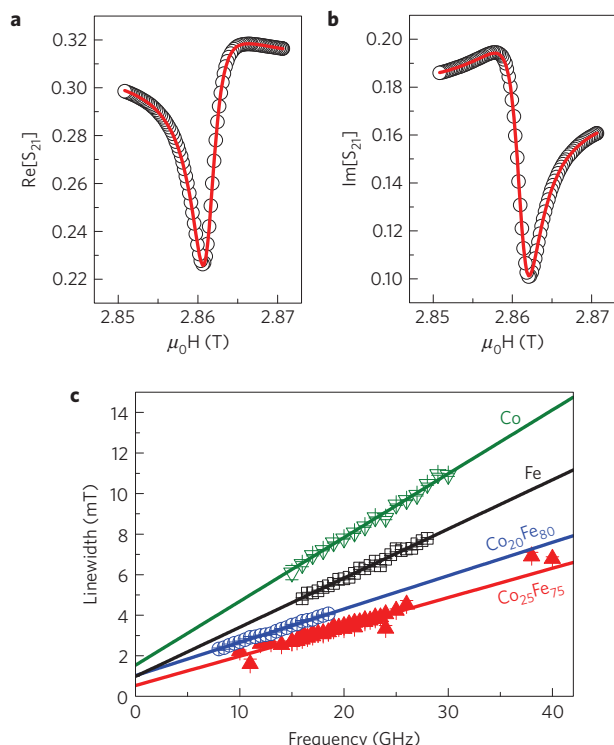


Figure 1 | Ferromagnetic resonance spectra, measured by means of FMR and the resulting linewidth as a function of frequency. a, b, Real and imaginary parts, respectively, of the $S_{21}(H)$ transmission parameter (open black circles) with the complex susceptibility fit (red lines). **c,** Linewidths (symbols) are plotted versus the frequency for Co, Fe, $\text{Co}_{20}\text{Fe}_{80}$ and $\text{Co}_{25}\text{Fe}_{75}$. The uncertainties in the linewidths were obtained by means of the standard method for the determination of confidence limits on estimated parameters for nonlinear models under the assumption of Gaussian white noise. The lines are error-weighted fits to equation (1), which are used to determine both the total damping α_{tot} and the inhomogeneous linewidth broadening for each alloy.

The measured total damping α_{tot} versus alloy composition for 10 nm films is plotted in Fig. 2. α_{tot} shows a clear minimum of $(2.1 \pm 0.1) \times 10^{-3}$ at a Co-concentration of 25%. However, as a result of the measurement geometry used and the structure of the sample, there are several extrinsic contributions to α_{tot} that are independent of α_{int} .

The first contribution—the result of the inductive coupling of the precessing magnetization and the co-planar waveguide (CPW)—is radiative damping α_{rad} (ref. 20). The FMR system is designed and optimized to couple microwaves into the ferromagnet, and therefore, by virtue of reciprocity, the system is efficient at coupling microwaves out of the ferromagnet. For very thin films or films with low saturation magnetization, α_{rad} is typically not a significant contribution to the total damping, and can be ignored. However, in the present case, α_{rad} must be accounted for in the analysis owing to the combination of a very high saturation magnetization and the exceptionally small value of α_{int} . As described in the Supplementary Section, we calculate and experimentally validate the contribution of α_{rad} to the total damping, which is plotted in Fig. 2.

The second non-negligible contribution to the total damping is the damping enhancement due to spin pumping into the adjacent Cu/Ta layers. The spin-pumping contribution α_{sp} can be determined from the thickness dependence of $(\alpha_{\text{tot}} - \alpha_{\text{rad}})$ because it behaves as an interfacial damping term²¹. Indeed, we measured the thickness dependence of $(\alpha_{\text{tot}} - \alpha_{\text{rad}})$ for many alloy samples to quantify and

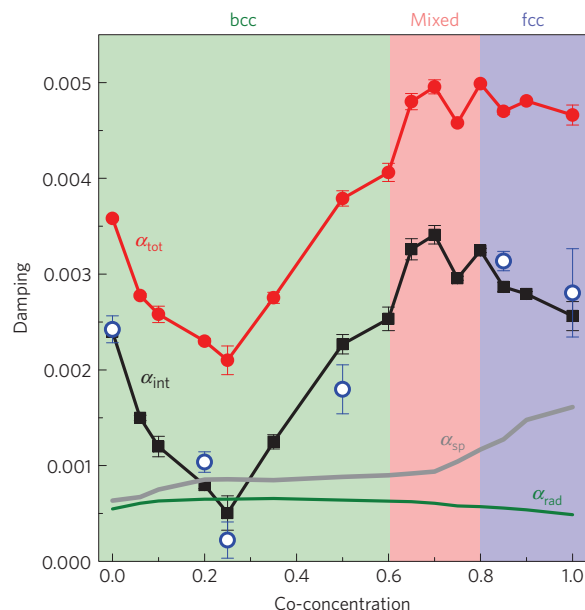


Figure 2 | Total measured damping with radiative and interfacial contributions. Total damping α_{tot} (red circles with lines), spin-pumping α_{sp} (grey line) and radiative α_{rad} (green line) contributions to the damping, the calculated intrinsic damping α_{int} (black squares with lines), as well as the extrapolated bulk value of the damping (blue open circles) are plotted as a function of Co-concentration. The errors of α_{tot} are determined from 95% confidence intervals of the error-weighted linewidth fits. The crystal structure of the alloys, obtained from XRD, is signified by the colour regions in the plot.

account for α_{sp} (see Supplementary Information), which is shown in Fig. 2.

Contributions from eddy-current damping²⁰ are estimated to be smaller than 5% and are neglected. Finally, two-magnon scattering is minimized in the perpendicular geometry used in this investigation, and its contribution is disregarded²².

The total measured damping becomes $\alpha_{\text{tot}} = \alpha_{\text{int}} + \alpha_{\text{rad}} + \alpha_{\text{sp}}$, allowing the intrinsic damping α_{int} to be determined, which is presented in Fig. 2. For many values of α_{int} , the contributions of α_{sp} and α_{rad} are of similar magnitude, showing the importance of accounting for these contributions. For the samples for which we have full thickness-dependent data, the intrinsic damping can also be determined from the y -intercepts found in the data of Supplementary Fig. 4. We also include these data in Fig. 2 (blue circles), which show that both approaches to remove the effects of spin pumping are consistent. For 25% Co, α_{int} now exhibits a sharp minimum in damping of $(5 \pm 1.8) \times 10^{-4}$, which is astonishing for a conductor. Indeed, values of $\alpha_{\text{int}} < 0.001$ have been measured only in ferrimagnetic insulators²³.

These results raise the question why α_{int} can be so low in the presence of conduction electrons. To gain a deeper understanding, we performed electronic structure calculations for $\text{Co}_x\text{Fe}_{1-x}$ within a full-relativistic, multiple-scattering approach (Korringa–Kohn–Rostoker method²⁴, KKR) using the coherent potential approximation (CPA)^{25,26} over the entire range of compositions (see Methods). Several representative examples are given in Fig. 3a.

The d -states (peak in the DOS below E_F) for pure Fe are not fully occupied. Consistent with the rigid band model²⁷, the d -states shift to lower energies when the concentration of Co increases, and become fully occupied at 25% Co, coinciding with the minimum in $n(E_F)$ shown in Fig. 3a, which originates from the hybridization between majority Fe e_g and minority Co t_{2g} states.

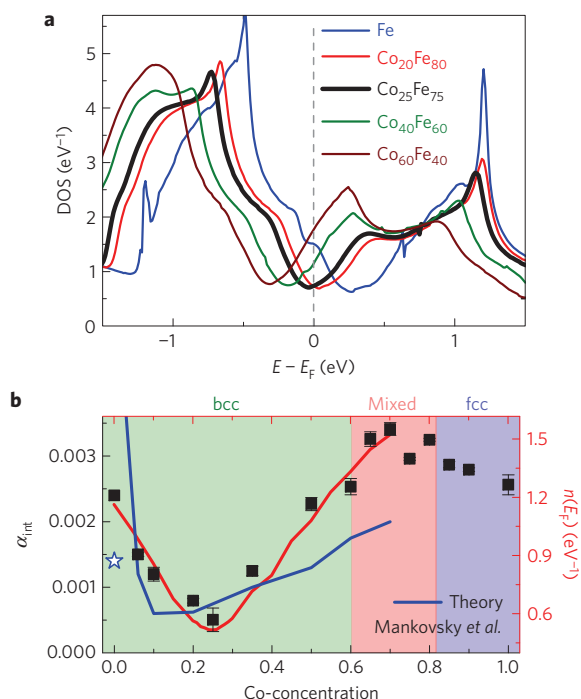


Figure 3 | Calculated electron density of states (DOS) and its comparison to the intrinsic damping. **a**, Electronic structure of bulk $\text{Co}_x\text{Fe}_{1-x}$. The DOS is shown for several Co-concentrations, as indicated. Note that all alloy compositions are aligned to a common Fermi energy, E_F , at zero energy to facilitate comparison. **b**, The intrinsic damping (black squares, left axis) is compared to the theory in Mankovsky *et al.*³, for a temperature of 0 K (blue line) and for a temperature of 300 K for pure Fe (blue star). The errors of α_{int} were obtained by summing the errors of α_{tot} and α_{sp} . The calculated DOS at the Fermi energy $n(E_F)$ is plotted on the right axis (red line). The y-offset of $n(E_F)$ is chosen deliberately to demonstrate that the concentration-dependent features of the damping directly correlate to features of $n(E_F)$. We cannot exclude concentration-independent contributions to the damping, which are accounted for by the 0.4 eV^{-1} y-offset.

Ebert *et al.*¹ and Lounis *et al.*²⁸ suggested that α_{int} is proportional to $n(E_F)$ in the breathing Fermi-surface model (that is, intraband transitions) in the cases of a minimally varying spin-orbit coupling (SOC) (as is the case for the $\text{Co}_x\text{Fe}_{1-x}$ system) and small electron-phonon coupling^{2,29}. Alternatively, interband transitions become significant only if bands have a finite overlap due to band broadening, caused for example by coupling to the phonons. As a result, interband transitions are suppressed at low temperature and energy dissipation becomes dominated by intraband transitions. Our RT measurements of $\text{Co}_x\text{Fe}_{1-x}$ satisfy this ‘low-temperature’ condition because the electron-phonon coupling is $<20 \text{ meV}$ for pure bcc Fe, and $<30 \text{ meV}$ for pure hcp Co. Band broadening due to disorder is about 15 meV for the e_g states that dominate at E_F (50 meV for the t_{2g} states) in $\text{Co}_{25}\text{Fe}_{75}$ and varies up to 55 meV for the e_g states (150 meV for the t_{2g} states) over the whole range of composition. These calculations show that the band-broadening effect at RT is too small to provide significant interband damping, consistent with the almost perfect proportionality between $n(E_F)$ for all alloy compositions in the bcc phase (0% to 60% Co). Such a proportionality requires an offset of 0.4 eV^{-1} , which originates from the fact the $n(E_F)$ is a superposition of all states, some of which do not contribute significantly to the damping.

The calculations of α_{int} by Mankovsky³ (included in Fig. 3b) show a minimum value of $\alpha_{\text{int}} \approx 0.0005$ between 10% and 20% Co, which differs in location from the sharp minimum we find at 25% Co

in both the experimental data and the calculated values of $n(E_F)$. Remarkably, with the exception of pure Fe, all calculated values of α_{int} (at 0 K) agree with our results within a factor of approximately two. Furthermore, the agreement is greatly improved for pure Fe when a finite temperature of 300 K is included (see Fig. 3b). Although not perfect, the agreement between those calculations and our results is compelling, and provides the critical feedback needed for further refinement of theory. In this regard, it is also worth noting the recent work by Turek *et al.*³⁰, since it gives a minimum for the calculated damping parameter at a concentration of 25% Co in close agreement with the measured damping parameter in Fig. 3 as well as the minimum in the DOS curve.

We therefore demonstrate and conclude that α_{int} is largely determined by $n(E_F)$ in the limit of intraband scattering. Second, our work shows that a theoretical understanding of damping requires an accurate account of all contributions to the damping parameter. Furthermore, the FeCo system studied here is unique from an electronic structure point of view, in the sense that the two elements have similar spin-orbit coupling and our calculations show that any enhanced broadening of electron states at the Fermi level due to alloying is small. The only remaining significant contributing factor to the damping is $n(E_F)$. Because all the other factors are relatively insensitive to the alloy composition and structure, the deep minimum in $n(E_F)$ for $\text{Co}_{25}\text{Fe}_{75}$ leads to the low intrinsic damping that we measure. If the theoretical explanation put forth here to explain low damping holds in general, it is natural to use data-mining algorithms to screen larger groups of materials to identify further low-damping systems. Examples of such studies to identify new materials for use, for example, in scintillators have been published³¹, and the generalization to applications in magnetization dynamics is straightforward.

Methods

Methods, including statements of data availability and any associated accession codes and references, are available in the [online version of this paper](#).

Received 14 December 2015; accepted 14 April 2016;
published online 16 May 2016

References

- Ebert, H., Mankovsky, S., Ködderitzsch, D. & Kelly, P. J. *Ab initio* calculation of the Gilbert damping parameter via the linear response formalism. *Phys. Rev. Lett.* **107**, 66603–66607 (2011).
- Gilmore, K., Idzerda, Y. U. & Stiles, M. D. Identification of the dominant precession-damping mechanism in Fe, Co, and Ni by first-principles calculations. *Phys. Rev. Lett.* **99**, 027204 (2007).
- Mankovsky, S., Ködderitzsch, D., Woltersdorf, G. & Ebert, H. First-principles calculation of the Gilbert damping parameter via the linear response formalism with application to magnetic transition metals and alloys. *Phys. Rev. B* **87**, 014430 (2013).
- Žutić, I., Fabian, J. & DasSarma, S. Spintronics: fundamentals and applications. *Rev. Mod. Phys.* **76**, 323–410 (2004).
- Emori, S., Bauer, U., Ahn, S.-M., Martinez, E. & Beach, G. S. D. Current-driven dynamics of chiral ferromagnetic domain walls. *Nature Mater.* **12**, 611–616 (2013).
- Jué, E. *et al.* Chiral damping of magnetic domain walls. *Nature Mater.* **15**, 272–277 (2016).
- Allivy Kelly, O. *et al.* Inverse spin Hall effect in nanometer-thick yttrium iron garnet/Pt system. *Appl. Phys. Lett.* **103**, 082408 (2013).
- Onbasli, M. C. *et al.* Pulsed laser deposition of epitaxial yttrium iron garnet films with low Gilbert damping and bulk-like magnetization. *APL Mater.* **2**, 106102 (2014).
- Kamberský, V. FMR linewidth and disorder in metals. *Czech. J. Phys. B* **34**, 1111–1124 (1984).
- Kamberský, V. On ferromagnetic resonance damping in metals. *Czech. J. Phys. B* **26**, 1366–1383 (1976).
- Kambersky, V. & Patton, C. E. Spin-wave relaxation and phenomenological damping in ferromagnetic resonance. *Phys. Rev. B* **11**, 2668–2672 (1975).

12. Thonig, D. & Henk, J. Gilbert damping tensor within the breathing Fermi surface model: anisotropy and non-locality. *New J. Phys.* **16**, 013032 (2014).
13. Brataas, A., Tserkovnyak, Y. & Bauer, G. E. W. Scattering theory of Gilbert damping. *Phys. Rev. Lett.* **101**, 037207 (2008).
14. Liu, Y., Starikov, A. A., Yuan, Z. & Kelly, P. J. First-principles calculations of magnetization relaxation in pure Fe, Co, and Ni with frozen thermal lattice disorder. *Phys. Rev. B* **84**, 014412 (2011).
15. Oogane, M. *et al.* Magnetic damping in ferromagnetic thin films. *Jpn. J. Appl. Phys.* **45**, 3889–3891 (2006).
16. Chang, H. *et al.* Nanometer-thick yttrium iron garnet films with extremely low damping. *IEEE Magn. Lett.* **5**, 6700204 (2014).
17. Liu, C., Mewes, C. K. A., Chshiev, M., Mewes, T. & Butler, W. H. Origin of low Gilbert damping in half metals. *Appl. Phys. Lett.* **95**, 022509 (2009).
18. Mizukami, S. *et al.* Low damping constant for CO₂FeAl Heusler alloy films and its correlation with density of states. *J. Appl. Phys.* **105**, 07D306 (2009).
19. Dürrenfeld, P. *et al.* Tunable damping, saturation magnetization, and exchange stiffness of half-Heusler NiMnSb thin films. *Phys. Rev. B* **92**, 214424 (2015).
20. Schoen, M. A. W., Shaw, J. M., Nembach, H. T., Weiler, M. & Silva, T. J. Radiative damping in waveguide-based ferromagnetic resonance measured via analysis of perpendicular standing spin waves in sputtered permalloy films. *Phys. Rev. B* **92**, 184417 (2015).
21. Tserkovnyak, Y., Brataas, A. & Bauer, G. E. W. Enhanced Gilbert damping in thin ferromagnetic films. *Phys. Rev. Lett.* **88**, 117601 (2002).
22. Hurben, M. J. & Patton, C. E. Theory of two magnon scattering microwave relaxation and ferromagnetic resonance linewidth in magnetic thin films. *J. Appl. Phys.* **83**, 4344–4365 (1998).
23. Sun, Y. *et al.* Damping in yttrium iron garnet nanoscale films capped by platinum. *Phys. Rev. Lett.* **111**, 106601 (2013).
24. Zabloudil, J., Hammerling, R., Szunyogh, L. & Weinberger, P. *Electron Scattering in Solid Matter* (Springer, 2005).
25. Durham, P. J., Gyorffy, B. L. & Pindor, A. J. On the fundamental equations of the Korringa–Kohn–Rostoker (KKR) version of the coherent potential approximation (CPA). *J. Phys. F* **10**, 661–668 (1980).
26. Faulkner, J. S. & Stocks, G. M. Calculating properties with the coherent-potential approximation. *Phys. Rev. B* **21**, 3222–3244 (1980).
27. Stern, E. A. Rigid-band model of alloys. *Phys. Rev.* **157**, 544–551 (1967).
28. Lounis, S., Santos Dias, M. dos & Schweefinghaus, B. Transverse dynamical magnetic susceptibilities from regular static density functional theory: evaluation of damping and g shifts of spin excitations. *Phys. Rev. B* **91**, 104420 (2015).
29. Kamberský, V. On the Landau–Lifshitz relaxation in ferromagnetic metals. *Can. J. Phys.* **48**, 2906–2911 (1970).
30. Turek, I., Kudrnovsky, J. & Drchal, V. Nonlocal torque operators in *ab initio* theory of the Gilbert damping in random ferromagnetic alloys. *Phys. Rev. B* **92**, 214407 (2015).
31. Ortiz, C., Eriksson, O. & Klintonberg, M. Data mining and accelerated electronic structure theory as a tool in the search for new functional materials. *Comput. Mater. Sci.* **44**, 1042–1049 (2009).

Acknowledgements

O.E. acknowledges support from the Swedish Research Council (VR) and the Knut and Alice Wallenberg Foundation (projects 2013.0020 and 2012.0031). DOS calculations were performed under a SNIC project.

Author contributions

M.A.W.S. and D.T. wrote the manuscript, J.M.S. and H.T.N. conceived of the experiment, M.A.W.S. deposited the samples, and performed the SQUID measurements and analysis, M.A.W.S., M.L.S. and H.T.N. performed the FMR measurements and analysis, J.M.S. performed the XRD measurements and analysis, D.T. and O.E. performed the first-principles DFT calculations. All authors contributed to the interpretation of the results.

Additional information

Supplementary information is available in the [online version of the paper](#). Reprints and permissions information is available online at www.nature.com/reprints. Correspondence and requests for materials should be addressed to J.M.S.

Competing financial interests

The authors declare no competing financial interests.

Methods

Sample preparation. The samples were deposited by DC magnetron sputtering at an Ar pressure of approximately 0.67 Pa (5×10^{-3} torr) in a chamber with a base pressure of less than 5×10^{-6} Pa (4×10^{-8} torr). The alloys were deposited by co-sputtering from two targets, with the deposition rates calibrated by X-ray reflectometry (XRR). The repeatability of the deposition rates was found to be better than 3% variation over the course of this study. For all deposited alloys, the combined deposition rate was kept at approximately 0.25 nm s^{-1} , to ensure similar growth conditions. Furthermore, the $\text{Co}_{30}\text{Fe}_{30}$ and the $\text{Co}_{25}\text{Fe}_{75}$ samples were replicated by depositing from single stoichiometric targets, to prove the reproducibility of the results. Samples with a thickness of 10 nm were fabricated over the full alloy composition range, and additional thickness series (7 nm, 4 nm, 3 nm and 2 nm) were fabricated for the pure elements and select intermediate alloy concentrations (20% Co, 25% Co, 50% Co and 85% Co).

X-ray diffraction measurement. The crystal structure of the alloys was determined by X-ray diffraction (XRD) using an in-plane geometry with parallel beam optics and a Cu K α X-ray source. The in-plane geometry allows the signal from the Co–Fe alloys to be isolated from the high-intensity signal coming from the silicon substrate. These measurements yield both the in-plane lattice constants and the crystal structure, as shown in the Supplementary Methods, Section 1. The deposition rates were calibrated by XRR using the same system as configured for the out-of-plane geometry.

Superconducting quantum interference device (SQUID) measurement. We measured the in-plane hysteresis curves at 300 K to determine the magnetic moment of the sample. Sample were first diced with a precision diamond saw such that an accurate value of the volume of the sample could be calculated. The saturation magnetization M_s for all alloy samples is then determined by normalizing the measured moment to the volume of Co–Fe in the sample. These values are shown in the Supplementary Methods.

VNA-FMR measurement. The FMR measurement used a room-temperature-bore superconducting magnet, capable of applying static magnetic fields as high as 3 T. An approximately 150 nm poly(methyl methacrylate) (PMMA) coat was first applied to the samples to prevent electrical shorting of the co-planar waveguide (CPW) and to protect the sample surface. Sample were placed face down on the CPW and microwave fields were applied in the plane of the sample, with frequencies that ranged from 10 GHz to 40 GHz. A vector network analyser (VNA) was connected to both sides of the CPW and the complex $S_{21}(H)$ transmission parameter was determined. The iterative susceptibility fit of $S_{21}(H)$ was done using the method described by Nembach and colleagues³². To minimize the fit residual, all fits were constrained to a field window that was three times the linewidth around the resonance field. We verified that this does not change the results, but reduces the influence of measurement noise on the error bars of the fitted values.

Calculation of the DOS. Electronic ground state calculations have been performed by a full-relativistic multiple-scattering Green's function method (Korringa–Kohn–Rostoker method²⁴, KKR) that relies on the local spin-density approximation (LDA) to density functional theory. We used Perdew–Wang exchange correlation functionals^{33–36}.

In our multiple-scattering theory, the electronic structure is described by scattering path operators $\tau_{ij}(i, j \text{ lattice site indices})$ ²⁴, where, in the spin-angular-momentum representation, we consider angular momenta up to $l_{\text{max}} = 3$ and up to $60 \times 60 \times 60$ points in reciprocal space. The substitutional alloys are treated within the coherent potential approximation (CPA)^{37,38}. Co impurities in the Fe host lattice are created in the effective CPA medium by defect matrices. The CPA medium is described by scattering path operators. The site-dependent potentials are considered in the atomic sphere approximation (potentials are spherically symmetric within muffin-tin spheres and constant in the interstitials).

The DOS is obtained from the integrated spectral density²⁴

$$n(E) = \frac{1}{\pi} \int_{\Omega_{\text{BZ}}} \text{Im}[\text{tr}(G(E + i\eta, \mathbf{k}))] d\mathbf{k}$$

with the small positive energy η . The integration in reciprocal space \mathbf{k} runs over the first Brillouin zone Ω_{BZ} .

Data availability. The data that support the plots within this paper and other findings of this study are available from the corresponding author on request.

References

32. Nembach, H. T. *et al.* Perpendicular ferromagnetic resonance measurements of damping and Lande g-factor in sputtered $(\text{Co}_2\text{Mn})_{1-x}\text{Ge}_x$ films. *Phys. Rev. B* **84**, 054424 (2011).
33. Becke, A. D. Density-functional exchange-energy approximation with correct asymptotic behavior. *Phys. Rev. A* **38**, 3098–3100 (1988).
34. Langreth, D. C. & Mehl, M. J. Beyond the local-density approximation in calculations of ground-state electronic properties. *Phys. Rev. B* **28**, 1809–1834 (1983).
35. Perdew, J. P. *et al.* Erratum: atoms, molecules, solids, and surfaces: applications of the generalized gradient approximation for exchange and correlation. *Phys. Rev. B* **48**, 4978 (1993).
36. Perdew, J. P. & Wang, Y. Accurate and simple analytic representation of the electron-gas correlation energy. *Phys. Rev. B* **45**, 13244–13249 (1992).
37. Asada, T. & Terakura, K. Generalized-gradient-approximation study of the magnetic and cohesive properties of bcc, fcc, and hcp Mn. *Phys. Rev. B* **47**, 15992–15995 (1993).
38. Paxton, A. T., Methfessel, M. & Polatoglou, H. M. Structural energy-volume relations in first-row transition metals. *Phys. Rev. B* **41**, 8127–8138 (1990).